Synchrotron Radiation News

ISSN: (Print) (Online) Journal homepage: https://www.tandfonline.com/loi/gsrn20

Operando X-ray Photoelectron Spectroscopy for High-Pressure Catalysis Research Using the POLARIS Endstation

David Degerman, Peter Amann, Christopher M. Goodwin, Patrick Lömker, Hsin-Yi Wang, Markus Soldemo, Mikhail Shipilin, Christoph Schlueter & Anders Nilsson

To cite this article: David Degerman, Peter Amann, Christopher M. Goodwin, Patrick Lömker, Hsin-Yi Wang, Markus Soldemo, Mikhail Shipilin, Christoph Schlueter & Anders Nilsson (2022) *Operando* X-ray Photoelectron Spectroscopy for High-Pressure Catalysis Research Using the POLARIS Endstation, Synchrotron Radiation News, 35:3, 11-18, DOI: 10.1080/08940886.2022.2078580

To link to this article: https://doi.org/10.1080/08940886.2022.2078580

OPEN ACCESS

TECHNICAL REPORT

Operando X-ray Photoelectron Spectroscopy for High-Pressure Catalysis Research Using the POLARIS Endstation

David Degerman,[1] Peter Amann,[1,2] Christopher M. Goodwin,[1] Patrick Lömker,[1,3] Hsin-Yi Wang,[1,4] Markus Soldemo,[5] Mikhail Shipilin,[1] Christoph Schlueter,[3] and Anders Nilsson[1]

[1]*Department of Physics, Stockholm University, AlbaNova University Center, Stockholm, Sweden*
[2]*Scienta Omicron AB, Uppsala, Sweden*
[3]*Photon Science, Deutches Elektronen Synchrotron DESY, Hamburg, Germany*
[4]*Enerpoly AB, Stockholm, Sweden*
[5]*PULSE Institute, SLAC National Accelerator Laboratory, Menlo Park, California, USA*
David Degerman *david.degerman@fysik.su.se*

Introduction

Climate change makes it essential that we develop alternatives to fossil-based resources for our energy and chemical needs. Production of fuels and chemicals from renewable sources can reduce or even eliminate CO_2 emissions, but it is necessary to find efficient ways to store and transmit energy. Synthetic fuels offer a promising alternative to fossil fuels as they offer the highest energy density of all energy storage media and can be stored cheaply over long periods. Today, fossil resources also form the basis of our current chemical industry with polymers, adhesives, lightweight carbon composites, detergents, and pharmaceuticals as a few examples, all consisting of carbon backbones. The chemical industry uses more than 10% of all fossil resources in Europe. Therefore, replacing the fossil feedstocks currently used in the chemical industry with sustainably produced base chemicals would significantly decrease net CO_2 emissions. The conversion of abundant molecules (in particular, water, CO_2, and N_2) into fuels and base chemicals (e.g., H_2, methanol, light olefins, aromatics, and ammonia) using renewable electricity and electrocatalysis, photocatalysis, or thermal catalysis is an essential component in a sustainable energy and chemical production system [1], as illustrated in Figure 1.

There currently exists scientific means to produce fuels and base chemicals from renewable electricity based on electrolysis to generate hydrogen combined with traditional thermal catalysis. However, no existing technology can do it sufficiently to be economically competitive with fossil resource-based processes. The scientific challenge is centered around molecular and interfacial catalysis. For thermal catalysis, the hydrogen feedstock derived via electrolysis would require processes at lower pressures (below 10 bar) and lower temperatures. It will be necessary to develop a new set of catalysts to reduce CO, CO_2, and N_2 into base chemicals and fuels at lower reaction conditions. Furthermore, we need new catalytic materials for electrocatalysis that can be selective towards specific products operating at low overpotentials.

To develop new catalytic materials, it is essential to derive a fundamental understanding of the active chemical phase and various reaction intermediates as the reaction occurs (*operando*) that can couple with theoretical simulations. This special issue illustrates how X-ray photoelectron spectroscopy (XPS) can be used to derive chemical information with high surface sensitivity. There are already many applications of differentially pumped near ambient pressure XPS (NAP-XPS) where surfaces can be probed under pressure of 0.1 mbar, and in exceptional cases pushed towards 10 mbar [2]. For investigating catalytic surfaces during CO, CO_2, and N_2 hydrogenation, at least 100–1000 times higher pressures are necessary since the reaction occurs at a temperature where otherwise the adsorbate population would be negligible. In order to meet this goal, we decided to develop the POLARIS instrument, an actual *operando* XPS technique for hydrogenation reactions.

The POLARIS instrument

The endstation POLARIS functions in some regards as most NAP-XPS instruments. A photograph of the instrument is shown in Figure 2a where one can see that it comprises a Scienta R4000 hemispherical analyzer equipped with a HiPP-2 differentially pumped pre-lens that separates a pressurized reaction volume from a vacuum regime using apertures in a thin titanium foil [3]. To fully explain the POLARIS instrument, however, we need to emphasize the aspects in which it differs from a conventional XPS endstation. Commonly in NAP-XPS instrumentation, a reaction cell is used. The chamber is set to a certain pressure through upstream mass flow controllers and downstream leak valves. Within the cell, a sample holder faces the inlet of the photoelectron analyzer (typically called "front cone" due to its shape). Some examples of this design include those in [4, 5]. The core of POLARIS uses a new and fundamentally different concept where the gas is blown straight onto the sample via a gas stream integrated into the front cone, as illustrated in Figure 2b. This creates a Ø2.5 mm and ~15–30 microm-

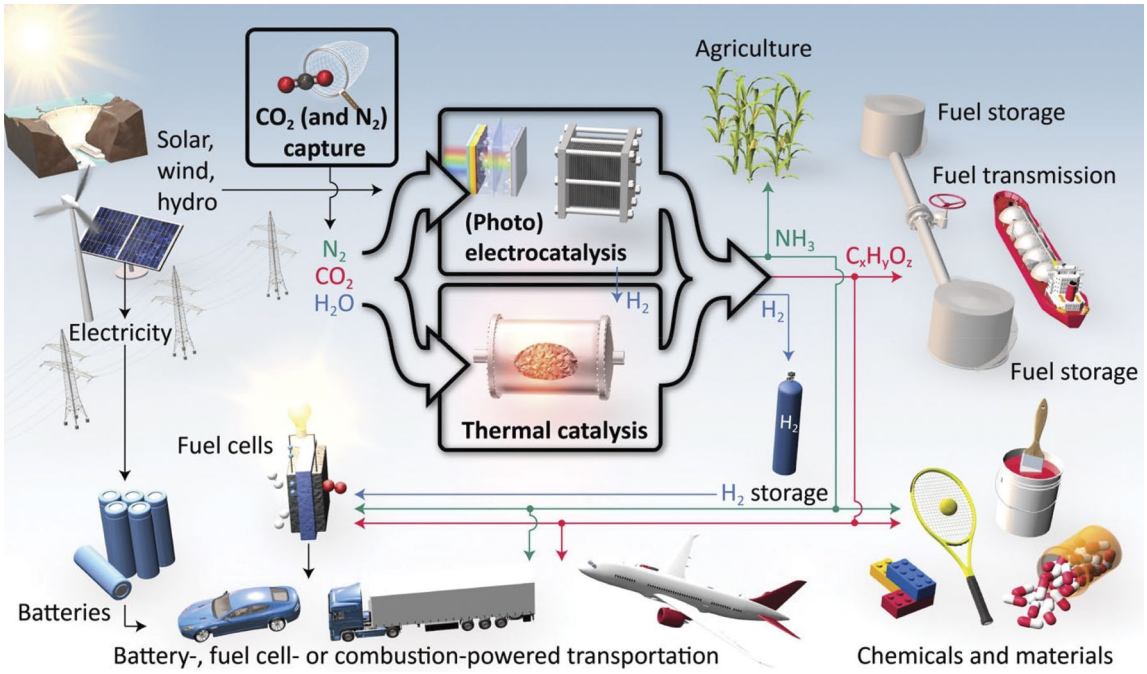

Figure 1. Illustration of a sustainable energy system to produce base chemicals for the industry and transportation fuel based on catalysis. Key processes are electrochemical water splitting and thermal and electrochemical CO_2 and N_2 reduction—graphics courtesy of Jakob Kibsgaard, DTU. An earlier version of this figure appeared in [1].

eter-thin cushion of pressurized gas just between the sample, and the analyzer inlet, where the sample is irradiated with X-rays and electrons are emitted. A rough vacuum (around 5–8 mbar) is maintained in the rest of the chamber by two 60 L/min fore-vacuum pumps (Kashiyama NeoDry Series). We use the name "virtual pressure cell" to describe this phenomenon of a pressurized but not confined gas volume. This cell development allows us to create overpressures beyond 1 bar in an otherwise UHV chamber in a simple way. The most relevant advantage of the virtual pressure cell compared to the traditional reaction cell is that the distance between the sample and the analyzer inlet is comparable to the inelastic mean free path (IMFP) of "tender X-ray" photoelectrons even at several hundreds of millibar pressure [6]. But several other benefits accompany this virtual cell development. For example, the proximity of the gas inlet and the X-ray interaction volume means that the pressure and gas composition at the gas inlet are always representative of the composition and pressure at the interaction point. Furthermore, since most of the gas entering the virtual cell is pumped away, the net flow of gases is away from the sample. This directionality results in low susceptibility to contaminants from the chamber walls and with higher gas flows at the surface, catalysts can be studied in the kinetic regime, not being mass-transfer limited. Moreover, the small volume of the virtual cell means that pressure or gas composition can be changed very rapidly (i.e., from 2 bar to 0), resulting in an instantaneous effect that opens opportunities for out-of-equilibrium experiments probed time-resolved with a time-resolution of 60 ms, limited by the 17 Hz frame rate of the detector camera [7]. Finally, the sample manipulation stage can be placed in a large experimental chamber and is thus not confined in the small reactor cell, which allows online alignment and manipulation of the sample with respect to the front cone.

Due to the very small distances and the virtual cell concept, it is not trivial to directly measure the pressure. Instead, we use a back-calibration method. Here, we pressurize the entire chamber with the intended gas mixture and correlate the chamber pressure to the pressure of the differential pumping stages. We can then track the pressure of the virtual cell pressure based on the continuous measurement of the differential stage pressure [3]. The pressure of the differential pumping stage is also used in a feedback loop controlling the sample manipulation stage in order to maintain the pressure to within 10 mbar of the desired pressure [8].

Normally, measurements of common catalytic adsorbates probe core levels such as C 1s, O 1s, and N 1s. In order to maximize the photoelectron cross-section, low photon energies <800 eV are typically chosen. The additional advantage of soft X-rays is increased surface sensitivity, since the photoelectrons do not have sufficient energy to escape the bulk. POLARIS once again turns this reasoning upside down. By utilizing significantly harder X-rays in the range between 2.4 and 10 keV, the IMFP of the photoelectrons increases significantly and allows better penetration of the gas phase. In order to maintain the surface sensitivity, it is an absolute necessity to be capable of achieving a grazing incidence angle below the critical angle for total exter-

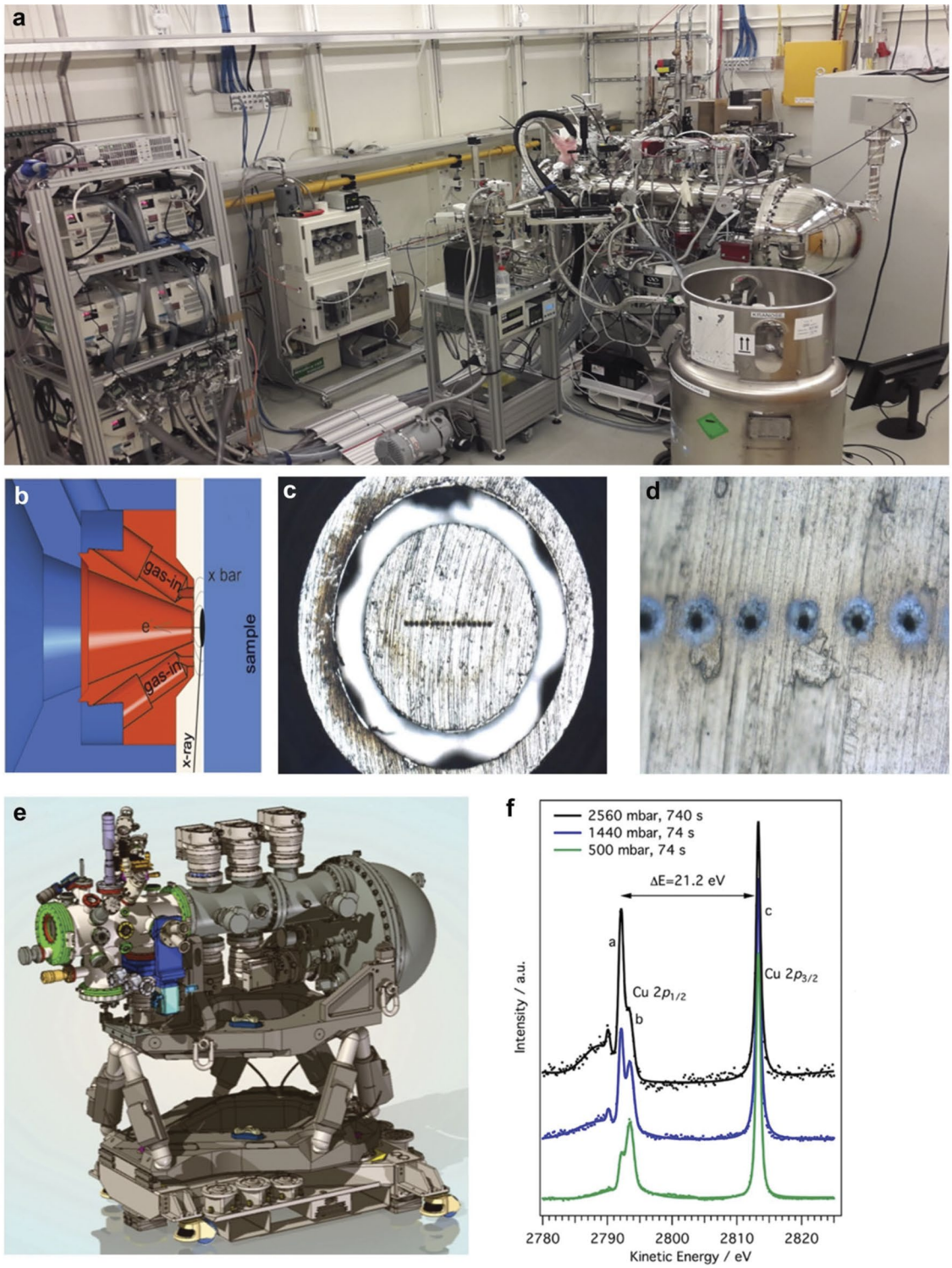

Figure 2. Illustrations of the POLARIS endstation. (a) The instrument on-site at beamline P22 at DESY, Germany. (b) A cut-through drawing of the front cone, which schematically illustrates the virtual cell concept. (c, d) Microscope images at two different zoom levels showing the array of apertures for the photoelectrons. (e) 3 D drawing of the instrument and the hexapod manipulator on which it stands. (f) Spectra of the Cu 2p region acquired at different pressures of He. The pressure and the integration times are indicated by the legend. The photon energy was 3.7 keV. The figure is adapted from Ref. [3].

nal reflection (typically well below one degree). Measuring below the critical angle allows the effective probing depth to be limited not by the IMFP of electrons in the solid, but rather by the penetration depth of the evanescent X-ray wave [9, 10]. With typical probing depths of ~15 Å, the coveted surface sensitivity can be maintained even with harder X-rays. Another advantage of the grazing incidence angle is that the footprint of the beam grows, which lowers the dose of photons per area unit of the sample. This advantage has, in experiments, proven crucial in order to avoid beam-induced chemistry. The design of the instrument has particularly been made to accommodate the grazing incidence geometry. The entire instrument, as is seen in Figure 2e, has been placed on top of a hexapod manipulation stage, which allows for translational and rotational movement in all degrees of freedom with sub-micrometer and microradian precision. Thus, we gain accurate control over the alignment with the X-ray beam and manipulation of the incidence angle during an ongoing experiment, as well as control over the incidence angle. The inlet of the analyzer is designed with the elongated beam footprint in mind, comprising an array of evenly spaced holes that maximizes the photoelectron transmission while simultaneously minimizing the gas transmission. This is illustrated in Figure 2c and d.

The beamline P22 at Petra III, Hamburg, Germany, complements the features of POLARIS extremely well [11, 12]. In order to realize the micrometer-scale distance between the sample and the front cone, also benefiting from the grazing incidence, the beamline has to provide a narrow beam focus (10 µm × 10 µm) and low divergence. Owing to the source's brilliance, the beamline is able to achieve the required foci with a horizontal divergence below 0.03° and flux in excess of 10^{12} photons/s at typical setups. The photon resolution selectable down to 150 meV using a combination of double crystal monochromator crystal and post monochromator. This tunability allows us to resolve relatively fine structures, such as chemical shifts in the C 1 s spectra dependent on the *x* in chemisorbed CH_x molecules, spin-orbit splitting in valence-like core levels such as Zn 3*d*, and surface-core-level shifts in Rh—all of these shifts are lower than 300 meV [13, 14].

A common way to gauge the strength of a high-pressure XPS setup is to test how high you can go in He pressure and still see a spectroscopic signal of the surface beneath the pressurized gas. In Figure 2f, we show this test with the Cu 2*p* core level in varying pressures up to 2.5 bar. In the figure, three peaks are identified. Peaks (b) and (c) are the spin-orbit split components, Cu $2p_{1/2}$ and Cu $2p_{3/2,}$ respectively. With higher pressure, the signal decreases as expected due to attenuation by the gas phase. Peak (a) is related to a peculiar kind of phenomenon where the photoelectron excites the electronic state of the He atom, resulting in a discreet but inelastic energy loss. In this case, we observe 1 *s* to 2*p* transition. Energy loss spectroscopy (EELS) measurements [15] of this transition agree well with the measured peak separation of 21.2 eV. We have observed similar unique molecular fingerprints of electron losses for every gas that we have used in the setup so far. In reactive mixtures, we have been able to follow CO oxidation at a total pressure of 1 bar [16].

Active phase in CO oxidation on Pd

Probing bulk metal peaks under a static pressure of inert gas are, however, not the main focus of this instrument. Here, we demonstrate how the accurate angle dependence of POLARIS can be used to derive the long-range structure of a Pd catalyst during CO oxidation using *Operando* XPS [10]. The surface structure is of particular interest in Pd due to the possibility of surface reconstructions and oxide formation during the catalytic reaction [17]. The question is the nature of the active phase: (1) the oxide on top of metallic Pd; (2) metallic islands are formed on top of the oxide; (3) the oxide is reduced and is exposing the bulk Pd in terms of pillars; or (4) a combination of (2) and (3). Here, grazing incidence XPS (GI-XPS) at different angles during reaction conditions can distinguish the different scenarios [10].

GI-XPS operates on the principle of total external reflection, wherein below the critical angle, the light source is reflected off the surface with a low penetration depth. At low angles, the X-ray light penetrates less deeply into the material; as the angle is increased, the penetration depth of the light increases. By calculating the penetration depth of the light and escape likelihood of the photoelectrons, the different models could be evaluated to determine the structure of the surface [9, 10].

Figure 3a shows an example of an incidence angle-resolved Pd $3d_{5/2}$ spectrum during CO oxidation at a total pressure of 300 mbar and a gas ratio of 50:4 O_2 to CO [10]. The metallic and oxide phases are well-resolved and are determined through curve fitting. Figure 3b shows the measured Pd/PdO intensity ratio as the incident angle of the X-rays relative to the surface is changed. When the incident angle of the photons approaches the critical angle, 0.7° for Pd at this photon energy, the X-ray field intensity within the sample changes. We clearly see a substantial variation in the ratio as the angle is changed. At low angles, below 0.2°, there is a strong metal signal that rapidly diminishes as the angle increases, forming a minimum in the ratio between 0.2° and 0.4°. At higher angles, the metal component then grows more rapidly again as for the very small angles, since we are above the critical angle, and probe the bulk metal more. This profile should be informative in terms of the nature of the Pd surface during CO oxidation and how the metal and oxide are distributed. By calculating the intensity of the field and including the effects of electron scattering through the different materials as a function of depth, a different model can be constructed where the fitting parameters are the thicknesses of the metal and oxide layers. Two of the models are shown in Figure 4b with either a fully covered surface with PdO or small Pd metal islands on the top pillars of PdO. It is the latter model that fits the experiment in a qualitative manner. Following Figure 4c, we conclude that small Pt metal islands form on top of the oxide and are the active phase during CO oxidations at realistic conditions of 300 mbar.

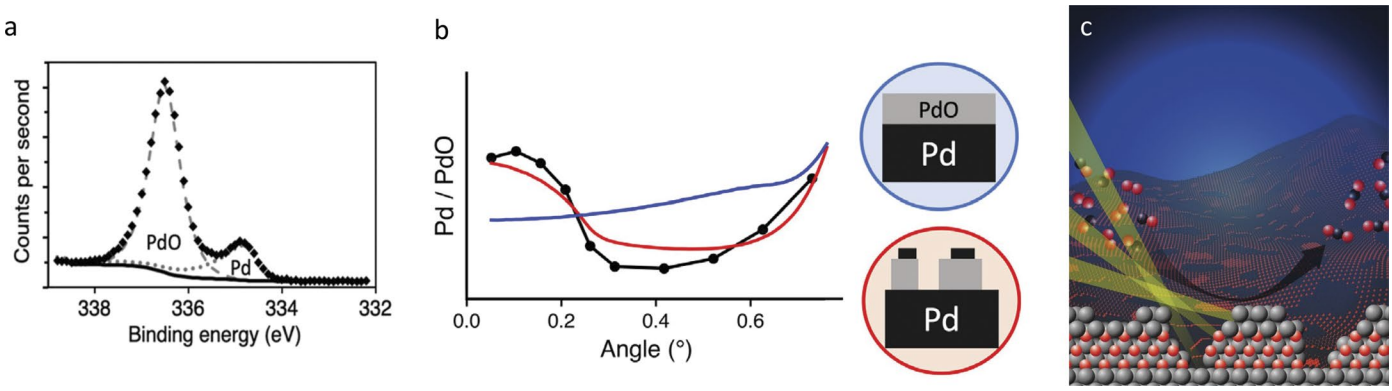

Figure 3. Operando XPS study of CO oxidation on Pd(100). (a) An example of peak fitting for the Pd $3d_{5/2}$ peak with two components, a metal peak based on pure components shown with a dotted line and an oxide with a dashed line. (b) Ratio of metal to oxide peak intensity as a function of angle with two calculated models. (c) Metallic Pd forms on top of PdO during the reaction. Reproduced from Ref. [10].

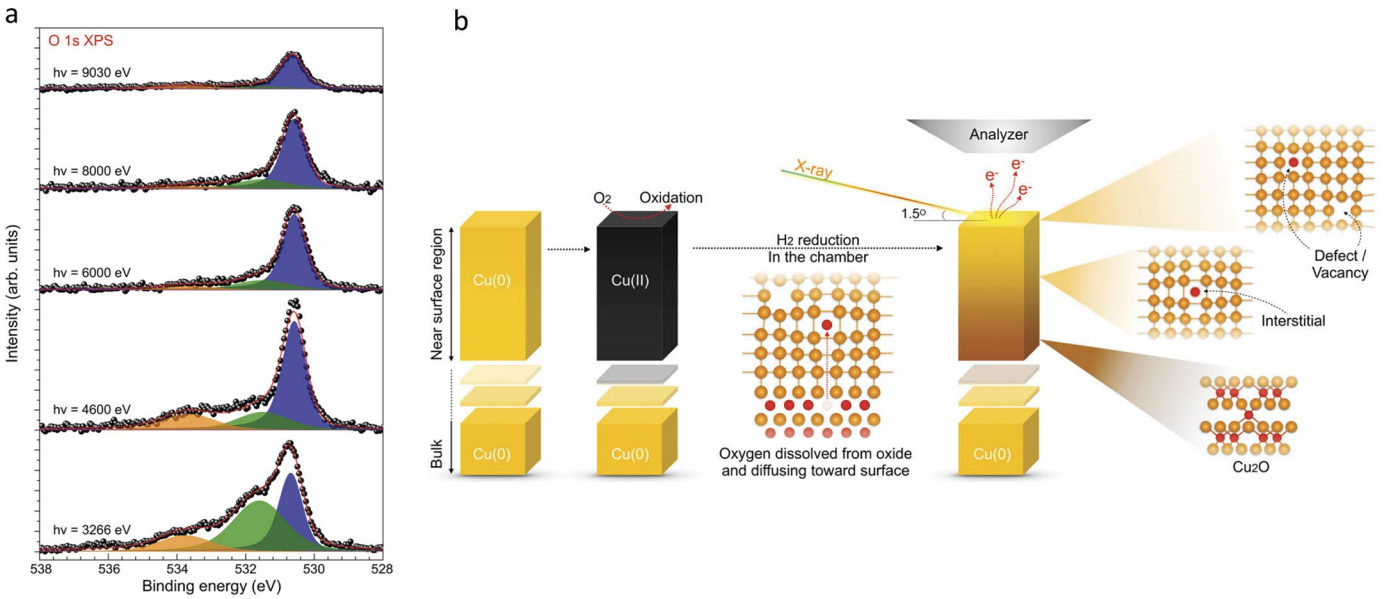

Figure 4: (a) Photon energy dependence of O 1 s XPS spectra after hydrogen treatment of oxidized Cu. The fitting results with blue: Cu_2O, green: $O_{Cu,vac}$, and orange: $O_{int.}$ (b) The illustration of two different subsurface oxygen species, $O_{Cu,vac.}$ and $O_{int.}$, formed during oxide-derived Cu preparation, where a defect/vacancy rich surface is generated by Cu atom rearrangement under H_2 treatment in the chamber, and the lattice oxygen is dissolved from the oxide and then diffuses toward to surface as O_{int}. Reproduced from Ref. [18].

Subsurface oxygen in a Cu catalyst

Among various catalysts that have been studied for electrochemical reduction of CO_2, Cu is the only pure metal capable of reducing CO_2 into higher-order hydrocarbons and oxygenates beyond the two-electron transfer products (e.g., formic acid or CO) in comparison to what has been observed on most other metals [19]. It is noteworthy that the activity and selectivity toward multi-carbon products of CO_2 reduction reaction can be significantly enhanced by fabricating a modified Cu by first oxidizing and subsequently reducing a pristine Cu substrate [20–22]. The origin of such improved performance on oxide-derived Cu has been discussed, but the particular related proposal here is that the enhanced performance is due to the appearance of subsurface oxygen [23, 24].

POLARIS was used to probe if subsurface oxygen could exist in the near-surface region of an oxidized Cu surface that has been reduced in-situ in H_2 at a pressure of 300 mbar and a temperature of 140 °C. After oxidation, the XPS spectrum showed the presence of Cu_2O and after reduction of Cu metal. Figure 4a shows the O 1 s photon energy-dependent XPS spectra at an incidence angle of 1.5° of the reduced Cu sample. Since different photon energies will generate photoelectrons with different kinetic energies, the sampling depth will vary. First, we directly observe that there is oxygen remaining in the sample. There

are three different spectral features that vary with photon energy, and their intensities have been determined using curve fitting. There are two distinctly different subsurface oxygen peaks, with one related to lattice defects/Cu vacancy (henceforth: $O_{Cu,vac}$) at 531.6 eV and interstitial oxygen (O_{int}) intercalated in the metallic Cu structure at 533.7 eV. There is also the dominating Cu_2O feature at 530.6 eV that still exists in the reduced sample.

The relative intensities show that at the most surface-sensitive probing photon energy of 3266 eV, the $O_{Cu,vac}$ is significantly stronger than O_{int}, but this difference is effectively removed when probing with 4600 eV photons. This strongly indicates that the $O_{Cu,vac}$ species is substantially more concentrated at the near-surface region than O_{int}, suggesting that interstitial oxygen is not stable near the surface in copper. During the reduction process, the metallic copper lattice gradually formed on top of Cu_2O will be defect-rich, and it will not order in a perfect fcc lattice structure. The O_{int} species is here thought of as the oxygen dissolved from Cu oxide that, upon interaction with copper lattice vacancy sites, may form $O_{Cu,vac}$. If it reaches the top-most surface

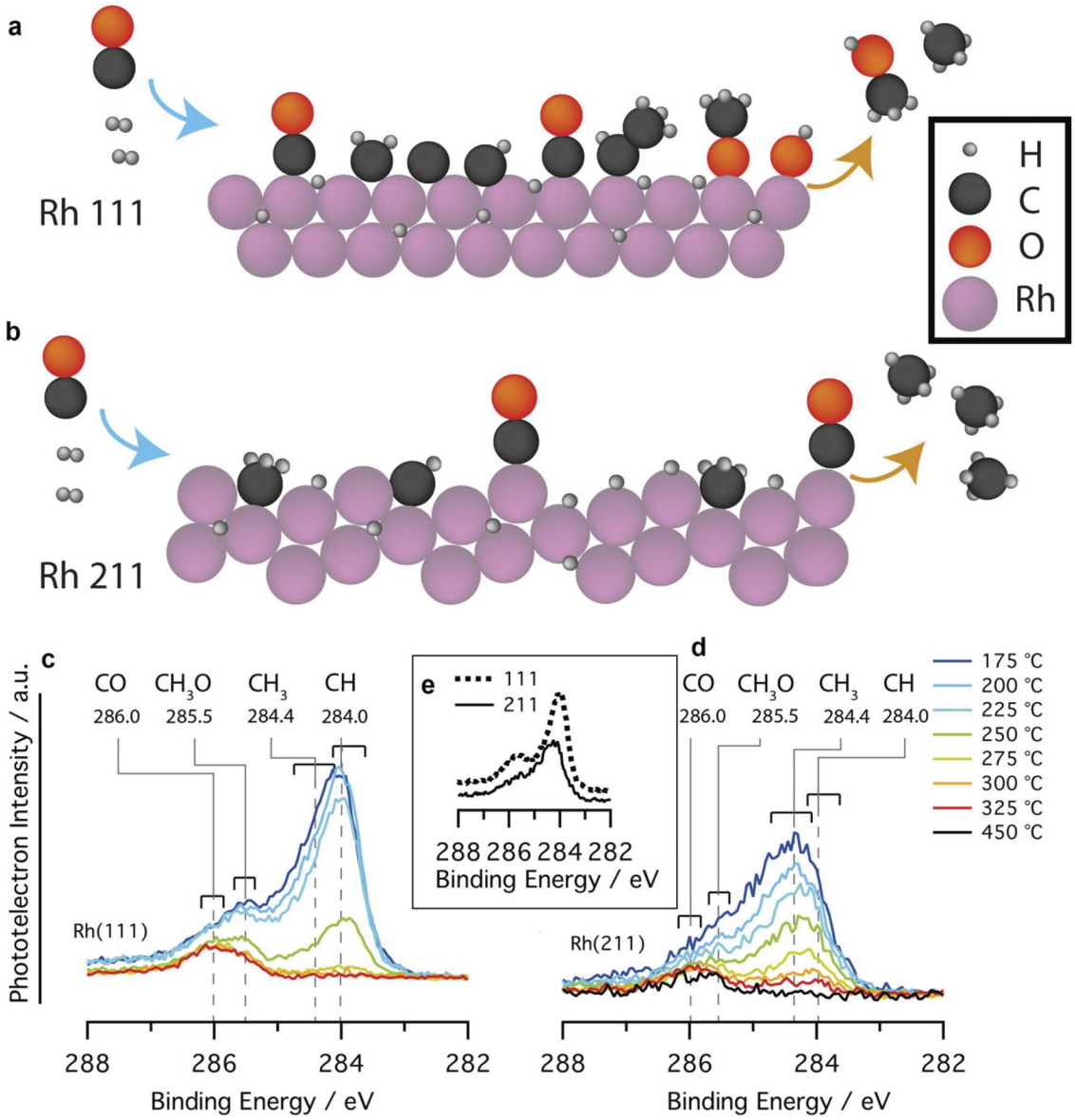

Figure 5: (a) An illustration of the chemical state of the Rh(111) surface. (b) A similar illustration for the Rh(211) surface. These are based on interpretations of the spectra shown in (c, d) of the C 1s region at the Rh(111) and Rh(211) surfaces, respectively. In inset (e), a comparison of the two surface orientations is shown at 225 °C. The photon energy in the experiment was 4.6 keV, and the CO: H_2 was flown at a 1:2 ratio and 150 mbar pressure. Figures adapted from Ref. [28].

region during reduction conditions, it will be reacted away. There is a Cu_2O layer buried underneath a reduced copper film, and this is based on the relative intensity changes as a function of photon energy and the dominating metallic copper signal in Cu spectra. The results here demonstrate that subsurface oxygen can exist in the near-surface region after a substantial reduction of the oxide and potentially affect the CO_2 electrochemical reduction by binding the intermediate CO much more strongly.

CO hydrogenation on rhodium

The target reactions to study with the POLARIS instrument are the hydrogenation reactions, such as thermal reduction of CO and CO_2. The mixture of CO, CO_2, and H_2, known as syngas, is a reaction mixture capable of revolutionizing the chemical industry by allowing synthesis of chemicals by basically performing backward combustion [25]. Rhodium is a particularly interesting catalyst since it has an inherent selectivity towards oxygenated hydrocarbons, which are coveted for their gravimetric and volumetric density [25–27]. But the hypotheses about the reaction mechanisms are numerous, and reliable confirmation is a perfectly posed question to be addressed by spectroscopic evaluation of the intermediates during an ongoing reaction.

With the help of POLARIS, we were able to see how the C 1 *s* region changes with reaction temperature at a working pressure of 150 mbar over single crystal catalysts cut along the (211) and (111) planes [28]. In Figure 5c w can clearly see how the distribution of adsorbates changes upon heating the sample by following the trend of four components. One component is located at 286.0 eV and corresponds to chemisorbed CO. Contrary to what was expected, the CO coverage stayed relatively unchanged in the whole temperature range, and we have found indications that the co-adsorption of H_2 forces a saturation coverage very much lower than otherwise seen in CO chemisorption [28]. The second component is located at 285.5 eV and corresponds to the methoxy radical CH_3O. Observation of this radical is consistent with the hypothesis that dissociation of the CO molecule occurs via the CH_3O intermediate on Rh(111) [26]. On the Rh(211) surface, the barriers for CO dissociation are lower, which causes the resting state of the catalyst to contain less CH_3O [28].

Lastly, we discuss the peak maxima of the significant components on the (211) and (111) surfaces, respectively. These correspond to hydrocarbon fragments, typically denoted CH_x, but with varying degrees of hydrogen saturation. On the Rh(211) surface, we observe a higher degree of hydrogen saturation; i.e., a resting state where most hydrocarbons are of the CH_3, or even $(CH_2)_x$–CH_3. On the Rh(111) surface, we observe a lower degree of hydrogen saturation of the hydrocarbons, mainly CH or hydrocarbons mostly containing C and CH monomers. The simultaneous observation of both oxygenates and CH_x species confirms that hydrogenation occurs both before and after the CO-bond dissociation step—a key hypothesis to explain the selectivity toward multicarbon oxygenates [25]. We further note that Rh(111) surface has better prerequisites for C–C-coupling than the Rh(211) surface, thanks to the lower degree of hydrogenation of the CH_x intermediates [28]. This is consistent with DFT modeling, predicting that the (111) surface is the most effective at converting syngas to oxygenates [29]. All conclusions are schematically summarized in Figure 5a–b.

Conclusion and outlook

We have shown an overview of the POLARIS instrument in conjunction with a set of examples where the spectroscopic insights from *operando* XPS and the unique features of POLARIS can contribute to answering pressing issues in the field of catalysis. As a first milestone, we plan to investigate transition metal catalysts used for various CO, CO_2, and N_2 hydrogenation reactions in a similar manner as we did for Rh. This model catalyst screening aims to provide spectroscopic observation of the different reaction mechanisms and better understand the surface chemical origin of their respective selectivities. As our understanding of the single crystal catalysts grows, we are expanding our investigations to include conventional nanoparticle catalysts and out-of-equilibrium systems, both using rapid pressure changes and femtosecond-resolved pump-probe experiments.

Funding

The development of the instrument and the research described within this article were funded by the Swedish Research Council (Vetenskapsrådet, VR) with award no 2013-8823, by the Swedish Foundation for Strategic Research (Stiftelsen för Strategisk Forskning, SSF) through award no 17-0034, and the Knut and Alice Wallenberg (KAW) Foundation (award no. 2016.0042). We acknowledge DESY (Hamburg, Germany), a member of the Helmholtz Association HGF, for the provision of experimental facilities. ■

References

1. Z. W. Seh et al., *Science* **355** (6321), eaad4998 (2017). doi:10.1126/science.aad4998
2. J. Schnadt et al., *J. Phys.: Condens. Matter.* **32** (41), 413003 (2020). doi:10.1088/1361-648X/ab9565
3. P. Amann et al., *Rev. Sci. Instrum.* **90** (10), 103102 (2019). doi:10.1063/1.5109321
4. M. E. Grass et al., *Rev. Sci. Instrum.* **81** (5), 053106 (2010). doi:10.1063/1.3427218
5. J. Knudsen et al., *Surf. Sci.* **646**, 160 (2016). doi:10.1016/j.susc.2015.10.038
6. S. Axnanda et al., *Sci. Rep.* **5**, 9788 (2015). doi:10.1038/srep09788
7. J. Knudsen et al., *Nat. Commun.* **12**, 1 (2021).
8. C. Goodwin et al., *Appl. Spectrosc.* **75** (2), 137 (2021). doi:10.1177/0003702820942798
9. L. G. Parratt, *Phys. Rev.* **95** (2), 359 (1954). doi:10.1103/PhysRev.95.359
10. C. M. Goodwin et al., *J. Phys. Chem. Lett.* **12** (18), 4461 (2021). doi:10.1021/acs.jpclett.1c00620
11. C. Schlueter et al., *AIP Conf. Proc.* **2054** (2019).
12. C. Schlueter et al., *Syncrotron Radiat. News* **31** (4), 29 (2018). doi:10.1080/08940886.2018.1483656
13. B. S. Bunnik, and G. J. Kramer, *J. Catal.* **242** (2), 309 (2006). doi:10.1016/j.jcat.2006.06.015
14. E. Vesselli et al., *J. Phys. Chem. C.* **112** (37), 14475 (2008). doi:10.1021/jp803112q
15. C. A. Walsh et al., *Philos. Mag. A Phys. Condens. Matter, Struct. Defects Mech. Prop.* **80**, 1507 (2000).

16. S. Blomberg et al. *ACS Catal.* **11** (15), 9128 (2021). doi:10.1021/acscatal.1c00806
17. M. Shipilin et al., *J. Phys. Chem. C.* **119** (27), 15469 (2015). doi:10.1021/acs.jpcc.5b04400
18. H. Y. Wang et al., *Angew. Chem. Int. Ed. Engl.* **61** (3), e202111021 (2022). doi:10.1002/anie.202111021
19. Y. Hori et al., *Electrochim. Acta* **39** (11–12), 1833 (1994). doi:10.1016/0013-4686(94)85172-7
20. F. S. Roberts et al., *Angew. Chem. Int. Ed.* **54** (17), 5179 (2015). doi:10.1002/anie.201412214
21. A. Eilert et al., *J. Phys. Chem. Lett.* **7** (8), 1466 (2016). doi:10.1021/acs.jpclett.6b00367
22. C. W. Li et al., *Nature* **508** (7497), 504 (2014). doi:10.1038/nature13249
23. F. Cavalca et al., *J. Phys. Chem. C.* **121** (45), 25003 (2017). doi:10.1021/acs.jpcc.7b08278
24. A. Eilert et al., *J. Phys. Chem. Lett.* **8** (1), 285 (2017). doi:10.1021/acs.jpclett.6b02273
25. H. T. Luk et al., *Chem. Soc. Rev.* **46** (5), 1358 (2017). doi:10.1039/C6CS00324A
26. Y. M. Choi, and P. Liu, *J. Am. Chem. Soc.* **131** (36), 13054 (2009). doi:10.1021/ja903013x
27. N. Yang et al., *J. Am. Chem. Soc.* **138** (11), 3705 (2016). doi:10.1021/jacs.5b12087
28. D. Degerman et al., *J. Am. Chem. Soc.* **144** (16), 7038 (2022).
29. J. Schumann et al., *ACS Catal.* **8** (4), 3447 (2018). doi:10.1021/acscatal.8b00201